 CMES, vol.33, no.1, pp.109-129, 2008

Computational Modeling of a Lightweight Composite Space Reflector using Geometrically Nonlinear Solid Shell Elements

K. Lee[1], C.T. Wu[2], G.V. Clarke[3] and S.W. Lee[4]

Abstract: A geometrically nonlinear finite element analysis of a low areal density composite space reflector is conducted under static conditions and the results are compared with independently carried out experimental data. The finite element analysis is based on an assumed strain formulation of a geometrically nonlinear nine-node solid shell element. Numerical results are in good agreement with experimental data. This demonstrates the effectiveness of the present solid shell element approach when applied to the analysis of highly flexible space structures. The results of numerical analysis and the experimental data reported in the present paper provide a benchmark for future investigations on the modeling and analysis of geometrically nonlinear composite shell structures via computational tools.

Keyword: Composite space reflector, assumed strain solid shell element, geometrically nonlinear analysis

1 Introduction

The areal density (mass/unit area) of the Hubble Space Telescope mirror, fabricated based on a glass facesheet and egg-crate construction is about 180 kg/m^2. Chen (1998) reported that the new generation of extremely lightweight composite reflectors can be produced at the areal density of 2 to 10 kg/m^2. In the development of a space telescope system the weight of the primary reflector is critical because it determines the type and weight of supporting structures, the overall payload and ultimately the cost. The lightweight, low cost structural composite mirrors have tremendous potential for enabling the Large Deployable Reflector (LDR), which was the key research initiative of the NASA Precision Segmented Reflector (PSR)

[1] Assistant Research Scientist, University of Maryland, College Park, MD, USA
[2] Assistant Professor, National Chiao-Tung University, Taiwan
[3] Formerly at NASA Goddard Space Flight Center, Greenbelt, MD, USA
[4] Professor, University of Maryland, College Park, MD, USA

program [Freeland, McElroy and Johnston (1989)]. One of the technological development challenges they identified includes the capability for generating realistic estimates of panel thermo-mechanical performance considering the composite material properties such as the number of laminate layers and fiber directions in the facesheet and the nonlinear behavior of the flexible composite reflector structure. Tompkins, Funk, Bowles, Towell and Connell (1992) have evaluated the thermal, mechanical and durability properties of twelve candidate materials for precision space reflector panel applications by exposing them to the simulated space environments. Connell and Abusafieh (2002) used graphite fiber reinforced composites to build reflector demonstrators due to low density and low coefficient of thermal expansion.

Lightweight space structures such as low areal density composite reflectors are highly flexible and may undergo large deflection under applied loadings, especially during the launch phase. A geometrically nonlinear analysis may be needed to determine the deformed shape for a clearance check and the stress and strain states to ensure structural integrity. The primary goal of the present study has been to investigate the feasibility of using finite element software based on a solid shell element formulation for analysis of highly flexible composite structures of radio-frequency space reflectors. A reliable analytical tool can help an analyst or a designer to examine various design options and reduce the number of hardware tests to validate a design.

The assumed-strain solid shell approach has been used successfully in modeling thin flat and curved structures undergoing large deflection. Lee and Pian (1978) introduced an independently assumed strain field to alleviate element locking problems. Since then, the assumed-strain approach was combined with the three-dimensional solid shell approach by [Ausserer and Lee (1988), Kim and Lee (1988)]. Kim and Lee (1988) introduced a modified constitutive law to incorporate physical behavior of thin shell structures. The solid shell element does not use rotational degrees of freedom to describe its geometry and kinematics of deformation. Accordingly, all kinematic variables are expressed in vector forms based on a global coordinate system. For a structure of complicated shape, this allows easy connections between substructures. Park, Cho and Lee (1995) used a set of benchmark problems to show that for geometrically nonlinear analysis, large load increments are possible with the solid shell approach, thereby increasing computational efficiency. Kemp, Cho and Lee (1998) and Lee, Cho and Lee (2002) improved the performance of the existing solid shell elements via combining the bubble function displacement with a carefully selected assumed strain field. In these studies, the results of numerical tests showed that the improved elements were significantly less sensitive to mesh distortion than the existing elements. Recently, Lee and Lee (2006)

investigated the applicability of the assumed-strain solid-shell approach to analysis of extremely thin structures. They showed that by using quadruple precision, one can significantly extend the effectiveness of the approach in terms of length-to-thickness ratio or radius-to-thickness ratio. Alternatively, researchers have used the Meshless methods for geometrically non-linear shell analyses in order to avoid the mesh distortion [Han, Rajendran and Atluri (2005), Sladek, Sladek, Wen and Aliabadi (2006) and Wen and Hon (2007)].

For the past two decades, the assumed-strain solid shell elements have been rigorously tested on various benchmark problems to validate improved element performance. In this study, we investigate the applicability of the improved solid shell element approach to effective analysis of highly flexible composite structures of complicated shape. The deformed configurations of a breadboard composite space reflector are determined under static conditions using a geometrically nonlinear solid shell finite element model based on the assumed strain formulation. Computational results are validated through comparisons with the data obtained from an independently conducted experiment.

2 Finite Element Formulation

In this section, the assumed strain solid shell element formulation for geometrically nonlinear analysis is briefly discussed. To reduce the sensitivity to the mesh distortion, the solid shell element is enhanced with the additional high-order, bubble function displacement.

2.1 The Solid Shell Elements

The solid shell element approach does not use rotational angles to describe kinematics of deformation. Accordingly, all kinematic variables are expressed in vector forms, based only on a global coordinate system. For a structure of complicated shape, this allows easy connections between substructures. In the solid-shell approach, the composite panel is treated as a three-dimensional solid, allowing thickness change and transverse shear deformation.

Figure 1 shows two versions of a solid shell element, one with eighteen nodes and the other with nine nodes. The eighteen-node version has three degrees of freedom per node while the nine-node version has six degrees of freedom per node. The two versions are equivalent to each other. The eighteen-node version can be used for three-dimensional analysis where multiple elements are needed through thickness. The nine-node version is convenient in modeling of thin shells, using single element through thickness.

In order to model curved thin shells such as the reflector, it is desirable to use a

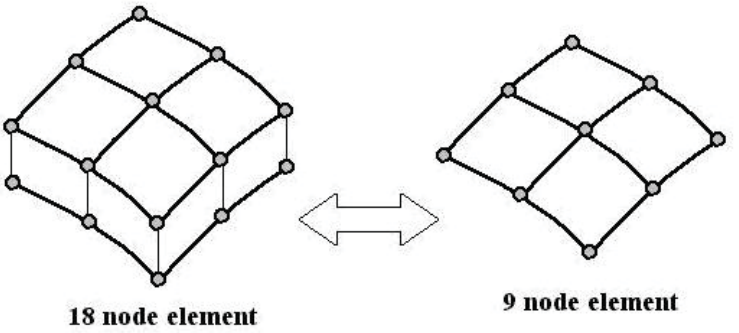

Figure 1: Eighteen-node and nine-node element

curved element such as the nine-node solid shell element in contrast to the simpler four-node element.

The performance of the nine-node element can be further enhanced by incorporating the bubble function displacement to make it less sensitive to the mesh distortion. The bubble function is a higher-order polynomial function that collapses to zero along the element boundary and at all its nodal points such that higher-order displacement can be represented inside the element. An assumed strain field corresponding to the introduced bubble function displacement vector is carefully chosen to avoid triggering any undesirable spurious kinematic modes [Lee, Cho, Lee (2002)]. The bubble function parameters are condensed out at the element level.

2.2 Geometrically Nonlinear Formulation

Geometrically nonlinear formulation is needed to account for large deflection. The formulation is based on the total Lagrangian description that employs Green strain and the second Piola-Kirchhoff stress. The finite element modeling results in an incremental equation for the Newton-Raphson iteration solution scheme, combined with the arc-length method. For geometrically nonlinear problems, the solid shell element approach allows load increments significantly larger than is possible with the conventional approach using rotational angles, resulting in an increased computational efficiency.

2.3 Assumed Strain Approach

The nine-node element used in the present study is based on the assumed strain formulation. Shell elements based on the assumed displacement alone suffer from ele-

ment locking. An assumed strain formulation uses an independently assumed strain field to alleviate the element locking [Lee and Pian (1978)]. In this approach, an assumed strain field is carefully chosen independently of the displacement-dependent strain field without triggering undesirable spurious kinematic modes. These two strain fields are related to each other via a compatibility equation. The assumed strain field within an element is expressed by assumed strain shape functions and their parameters that are eliminated at the element level. Accordingly, these additional assumed strain parameters do not increase the number of unknowns at the global level. Detailed description of the assumed strain solid shell formulation has been provided by Park, Cho and Lee (1995) and Kim and Lee (1988).

2.4 Incremental Formulations

For a solid in equilibrium,

$$\int_V \delta\bar{\boldsymbol{\varepsilon}}^T \boldsymbol{\sigma} dV - \delta W = 0 \tag{1}$$

where $\boldsymbol{\sigma}$ is the second Piola-Kirchhoff stress vector, $\delta\bar{\boldsymbol{\varepsilon}}$ is the virtual displacement-dependent strain vector, δW is the virtual work due to the applied load and V represents the volume of the original configuration.

For shells, the displacement-dependent strain vector can be expressed as

$$\bar{\boldsymbol{\varepsilon}} = \bar{\boldsymbol{\varepsilon}}_0 + \varsigma\bar{\boldsymbol{\varepsilon}}_1 \tag{2}$$

where ς is a non-dimensional parent coordinate in the thickness direction. Note that the over-bar is used for displacement-dependent quantities in this paper. In incremental form the displacement-dependent strain vector $\bar{\boldsymbol{\varepsilon}}$ can be written symbolically as follows:

$$\bar{\boldsymbol{\varepsilon}} = {}^{(n)}\bar{\boldsymbol{\varepsilon}}_0 + \Delta\bar{\mathbf{e}}_0 + \Delta\bar{\mathbf{h}}_0 + \varsigma({}^{(n)}\bar{\boldsymbol{\varepsilon}}_1 + \Delta\bar{\mathbf{e}}_1 + \Delta\bar{\mathbf{h}}_1) \tag{3}$$

where the left superscript (n) indicates the current state, and $\Delta\bar{\mathbf{e}}_{0,1}$ and $\Delta\bar{\mathbf{h}}_{0,1}$ are the incremental strain vectors that are linear and quadratic in incremental displacement respectively. Introducing the assumed displacement, incremental strain vectors in equation (3) that are linear in incremental displacement can be expressed in matrix form as follows:

$$\begin{aligned} \Delta\bar{\mathbf{e}}_0 &= \mathbf{B}_0(\xi,\eta)\Delta\mathbf{q}_e \\ \Delta\bar{\mathbf{e}}_1 &= \mathbf{B}_1(\xi,\eta)\Delta\mathbf{q}_e \end{aligned} \tag{4}$$

where ξ,η are the non-dimensional parent coordinates in the shell midsurface, and the incremental element DOF vector $\Delta\mathbf{q}_e$ includes the bubble function parameters.

2.4.1 Option #1

The displacement-independent strain $\boldsymbol{\varepsilon}$ is assumed to be linear in the thickness direction such that

$$\boldsymbol{\varepsilon} = \boldsymbol{\varepsilon}_0 + \varsigma \boldsymbol{\varepsilon}_1 \tag{5}$$

The stress vector is then related to the independently assumed strain vector such that

$$\boldsymbol{\sigma} = \mathbf{C}\boldsymbol{\varepsilon} \tag{6}$$

where $\mathbf{C}$ is the matrix of linear elastic stiffness constants. The independently assumed strain vector $\boldsymbol{\varepsilon}$ can be related to the displacement-dependent strain vector $\bar{\boldsymbol{\varepsilon}}$ via using the compatibility equation as

$$\int_{V_e} \delta\boldsymbol{\varepsilon}^T \mathbf{C}(\boldsymbol{\varepsilon} - \bar{\boldsymbol{\varepsilon}}) dV = 0 \tag{7}$$

where V_e is the element volume. The assumed strain vector can be expressed symbolically in matrix form as

$$\boldsymbol{\varepsilon} = \mathbf{P}_0(\xi, \eta)\boldsymbol{\alpha}_0 + \varsigma \mathbf{P}_1(\xi, \eta)\boldsymbol{\alpha}_1 \tag{8}$$

where $\mathbf{P}_0$, $\mathbf{P}_1$ are the assumed strain shape function matrices for the ς–independent and ς–dependent strain vectors, respectively and $\boldsymbol{\alpha}_0$, $\boldsymbol{\alpha}_1$ are vectors of the corresponding assumed strain parameters. For the nine-node element with the bubble function displacement, a detailed description of this option has been provided by Lee, Cho and Lee (2002).

2.4.2 Option #2

Element locking is associated with the ς–independent part of the strain. Accordingly, one may introduce an assumed strain field only for the ς–independent strain vector to obtain essentially the same performance as the first option such that

$$\boldsymbol{\varepsilon} = \boldsymbol{\varepsilon}_0 + \varsigma \bar{\boldsymbol{\varepsilon}}_1 \tag{9}$$

with

$$\boldsymbol{\varepsilon}_0 = \mathbf{P}_0(\xi, \eta)\boldsymbol{\alpha}_0 \tag{10}$$

Then, equation (9) can be rewritten symbolically as follows:

$$\boldsymbol{\varepsilon} = \mathbf{P}_0(\xi, \eta)\boldsymbol{\alpha}_0 + \varsigma \bar{\boldsymbol{\varepsilon}}_1 \tag{11}$$

In incremental form,

$$\Delta\boldsymbol{\varepsilon} = \mathbf{P}_0(\xi,\eta)\Delta\boldsymbol{\alpha}_0 + \varsigma\Delta\bar{\boldsymbol{\varepsilon}}_1 \tag{12}$$

Similar to the option #1, one may relate the independently assumed strain vector $\boldsymbol{\varepsilon}_0$ to the displacement-dependent strain vector $\bar{\boldsymbol{\varepsilon}}_0$ via using the compatibility equation as

$$\int_{V_e} \delta\boldsymbol{\varepsilon}_0^T \mathbf{C}(\boldsymbol{\varepsilon}_0 - \bar{\boldsymbol{\varepsilon}}_0)dV = 0 \tag{13}$$

In incremental form, the ς–independent strain vector is

$$\Delta\boldsymbol{\varepsilon}_0 = \mathbf{P}_0(\xi,\eta)\Delta\boldsymbol{\alpha}_0 \tag{14}$$

and the virtual independent strain vector is set as

$$\delta\boldsymbol{\varepsilon}_0 = \mathbf{P}_0(\xi,\eta)\delta\boldsymbol{\alpha}_0 \tag{15}$$

Substituting the appropriate strain terms in the equations (3), (4), (14) and (15) into the equation (13) and neglecting the higher order terms in the incremental displacement vector leads to

$$\mathbf{H}_0\Delta\boldsymbol{\alpha}_0 - \mathbf{F}_0 - \mathbf{G}_0\Delta\mathbf{q}_e = 0 \tag{16}$$

where

$$\begin{aligned}
\mathbf{F}_0 &= \int_{A_e} \mathbf{P}_0^T \mathbf{C}_0({}^{(n)}\bar{\boldsymbol{\varepsilon}}_0 - {}^{(n)}\boldsymbol{\varepsilon}_0)dA \\
\mathbf{G}_0 &= \int_{A_e} \mathbf{P}_0^T \mathbf{C}_0\mathbf{B}_0 dA \\
\mathbf{H}_0 &= \int_{A_e} \mathbf{P}_0^T \mathbf{C}_0\mathbf{P}_0 dA
\end{aligned} \tag{17}$$

Note that the volume integral in equation (13) has been transformed to the area integral in equation (17). This can be done via assuming that the determinant J of the Jacobian matrix is linear in ς as follows:

$$J(\xi,\eta,\varsigma) = J_0(\xi,\eta) + \varsigma J_1(\xi,\eta) \tag{18}$$

With the above assumption, one can introduce the following relation

$$\mathrm{d}V = (1 + r\varsigma)\mathrm{d}\varsigma dA \tag{19}$$

where $r(\xi,\eta)=J_1/J_0$. Equation (18) allows analytical integration through the shell thickness. The $\mathbf{C}_0$ matrix in equation (17) is obtained by analytically integrating the $\mathbf{C}$ matrix through the thickness as

$$\mathbf{C}_0 = \int \mathbf{C}(1+r\varsigma)d\varsigma \tag{20}$$

This feature is convenient in modeling of laminated composite structures [Kim and Lee (1988)].

From equation (16), one can determine the incremental vector of the assumed strain parameters as

$$\Delta\boldsymbol{\alpha}_0 = \mathbf{H}_0^{-1}(\mathbf{G}_0\Delta\mathbf{q}_e + \mathbf{F}_0) \tag{21}$$

Substituting equation (21) into equation (14), one can express the incremental assumed strain vector in equation (12) as follows:

$$\Delta\boldsymbol{\varepsilon} = \hat{\mathbf{B}}_0\Delta\mathbf{q}_e + \mathbf{P}_0\mathbf{H}_0^{-1}\mathbf{F}_0 + \varsigma\Delta\bar{\boldsymbol{\varepsilon}}_1 \tag{22}$$

where

$$\hat{\mathbf{B}}_0 = \mathbf{P}_0\mathbf{H}_0^{-1}\mathbf{G}_0 \tag{23}$$

One can then introduce equation (22) in the incremental form of the equilibrium in equation (1). The bubble function parameters as well as the assumed strain parameters are eliminated at the element level to derive the incremental equation for unknown incremental nodal degrees of freedom.

3 Composite Space Reflector

As shown in Fig. 2, the space reflector consists of a dish and a stiffener. The stiffener is composed of a frame and a cap. The thickness of the dish is very small relative to other dimensions. For example, the ratio of the greatest distance between two points on the dish edges to its thickness is about three thousand. However, this ratio is still well below the working limit of the assumed strain solid shell element which is about one million according to the recent study by Lee and Lee (2006).

The reflector is fixed at three points on the top of the three short columns as shown in Fig. 3. A loading arm installed for the experiment is shown at the lower right corner.

Figure 4 shows a bottom view of the finite element model for the reflector. The reflector dish was manufactured in four separate parts and bonded together over the

Figure 2: Composite space reflector

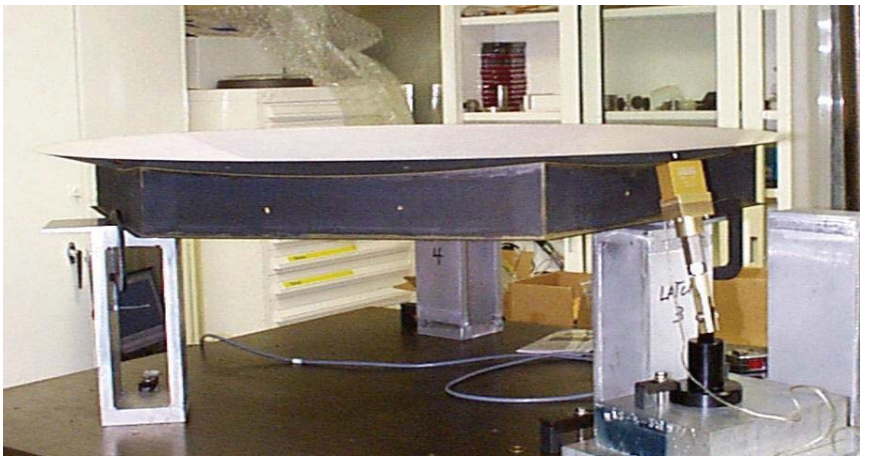

Figure 3: Side view of the reflector

Figure 4: Finite element model for the reflector

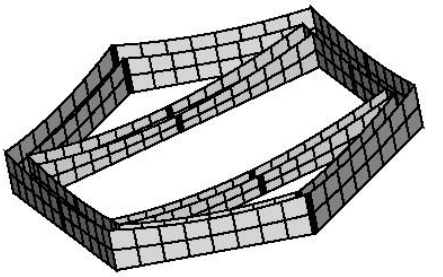

Figure 5: Stiffener (Frame)

two narrow bands that form a cross. Accordingly, the overlapped region is twice as thick, while the doubly overlapped region at the center of the reflector dish is four times as thick as the remaining area.

The stiffener of the reflector is composed of a frame and a cap as shown in the following figures. The frame consists of thin panels that are connected to form two hexagons, inner and outer, as shown in Figure 5. A pair of two straight strips is attached to the inner hexagon to help maintain the hexagonal shape and also support the reflector dish. The thickness of the frame is one and half times the dish thickness.

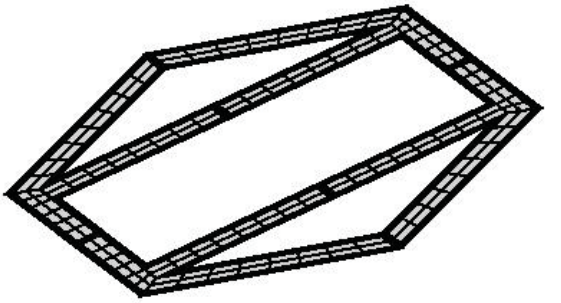

Figure 6: Stiffener (Cap)

The cap shown in Fig. 6 is attached to the bottom of the frame so that the cross sections of the stiffener form closed cells to enhance the structural rigidity.

3.1 The Reflector Geometry

The reflector dish is described by a parabolic equation based on the coordinate system as shown in Figure 7. Note that the coordinate system shown in the figure is different from the system used for finite element modeling. A cutting plane with an angle of 22˚ and a cut-offset of 8.615" is introduced to define the dish surface, which is shown as the curved line A-B on the parabola. These geometric data were obtained from the manufacturer.

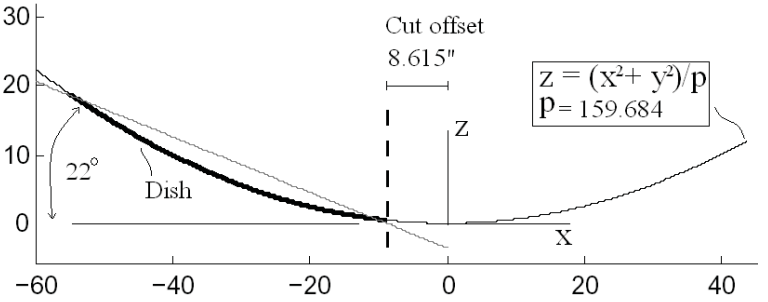

Figure 7: Parabolic cross-sectional shape, cut-offset and angle

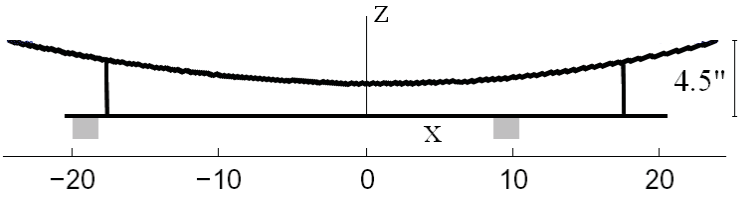

Figure 8: Side view of the reflector

Other geometric parameters needed for the finite element modeling were measured from the actual reflector due to a lack of drawing data. They are shown in Figs. 8, 9, and 10. The maximum height of the dish from the base is measured 4.5" as shown in Fig 8.

Figure 9 shows a top view of the dish. For simplicity, only a half of the dish is shown. The overlapped zone is 0.032" thick and 0.625" wide while the doubly overlapped zone at the center is 0.064" thick and 0.625" wide.

Figure 10 shows a top-view of the finite element model of the cap with the measured geometric data. For simplicity, only one quarter of the cap is shown. One

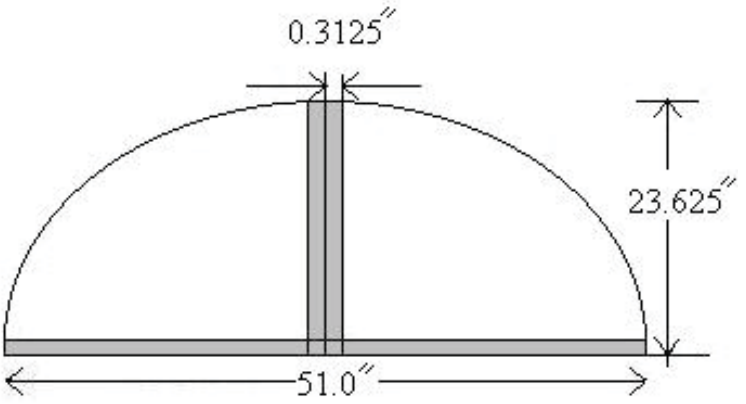

Figure 9: Top view of a half dish

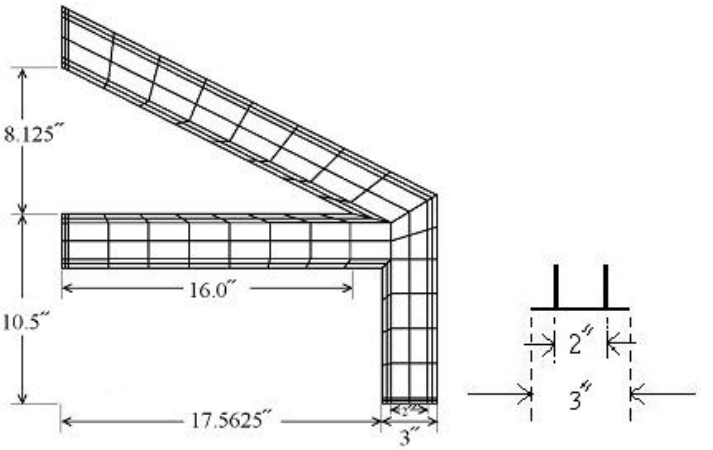

Figure 10: Measurements of the cap

may notice that three elements are used in the width direction to accommodate the connection with the frame. The sketch on the right-hand side shows a stiffener cross-section.

The reflector dish is symmetric with respect to the x-axis as shown in Fig. 11, but non-symmetric with respect to y-axis. The lowest point in the dish is biased slightly toward the positive x-direction as shown in the A-A section view of Fig. 11. The global x, y, z-coordinate system shown in the figure is used for the finite element modeling. The origin of x-axis is located at the mid-point of line A-A. The reflector is fixed to the base at the three attaching points on the bottom surface of the cap as

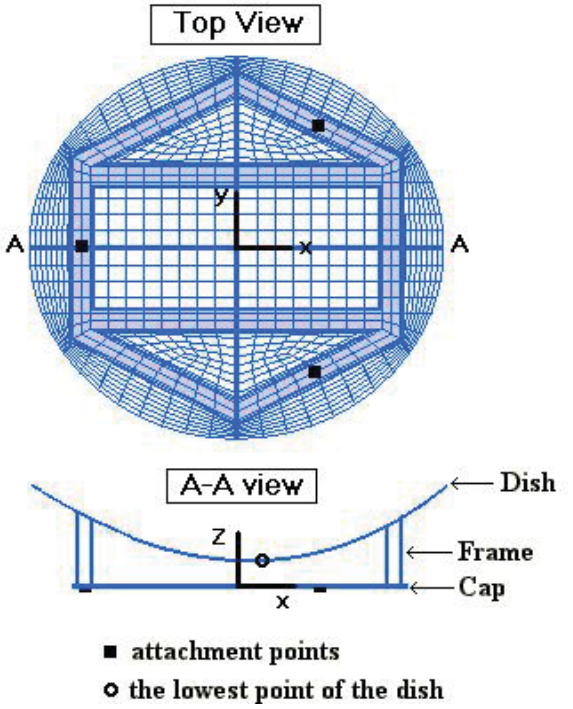

Figure 11: Top and A-A section view

shown in the figure.

3.2 Composite Material Properties

The reflector dish and stiffeners are all constructed of composite materials. The material properties provided by the manufacturer are shown in Tab. 1. For convenience, a ply axis system of 1-2-3 is used to describe the material properties where the axis 1 represents the fiber direction, axis 2 represents the transverse direction and axis 3 represents the thickness direction. The moduli of the materials are dependent on the loading direction. For example, extensional modulus E_1 in the fiber direction is 53.0 Msi in tension and 50.0 Msi in compression.

For the dish, a quasi-isotropic, 8-ply, symmetric layup of $[0/90/45/\text{-}45]_s$ is used, while for the stiffener, a quasi-isotropic, 12-ply, doubly symmetric layup of $[0/60/\text{-}60]_{s2}$ is used. The angles are measured with respect to the laminate axis. The dish is 0.016" thick and the stiffener is 0.024" thick.

Table 1: Material Constants

E_1	53.0 Msi (tension)	50.0 Msi (compression)	
E_2,E_3	0.95 Msi (tension)	0.91 Msi (compression)	
ν_{12}, ν_{13}	0.319	ν_{23}	0.46
G_{12},G_{13}	0.681 Msi	G_{23}	0.31849 Msi

4 Geometrically Nonlinear Static Analyses

A mesh generator tailored for analysis of the reflector has been implemented. One may note that because of the complicated shapes, the mesh distortion is severe in the triangular zones of Fig. 12 enclosed by the inner frame. The improved nine-node elements based on the bubble function displacement, insensitive to the mesh distortion, are used for this reason. The geometrically nonlinear analysis is carried out for the three load cases shown in Fig. 12, using the option 1 version of the assumed strain solid shell formulation. In each case, a point load is applied perpendicular to the original, undeformed surface of the dish and the direction of the load remains fixed during deformation. The E_1 and E_2 values measured under tensile condition are chosen for analysis. The results of the analysis are compared with the experimental data.

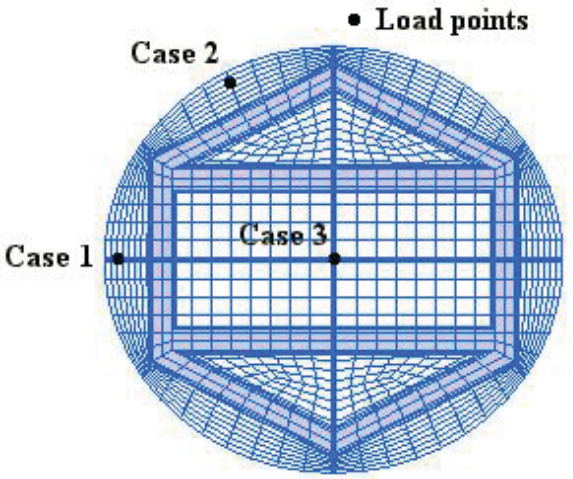

Figure 12: Three cases of point load

4.1 Loading Case 1

A point load perpendicular to the surface of the dish is applied at a nodal point shown in Fig. 13. For convenience, the figure shows only one quarter of the mesh for the reflector. The load point is located within the overlapped region, modeled by a fine mesh.

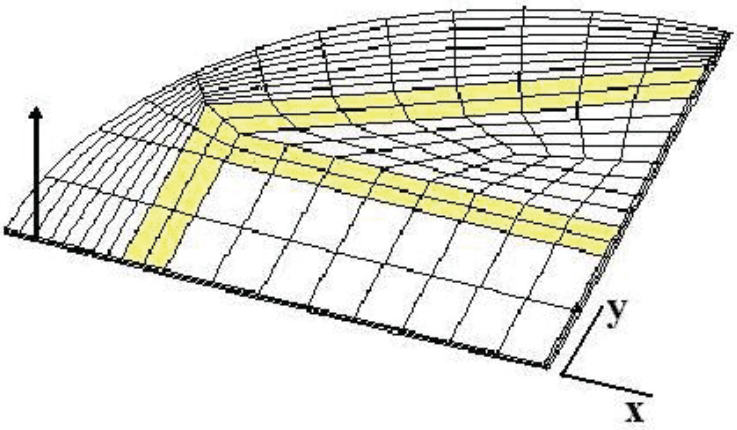

Figure 13: Load direction and mesh for case 1

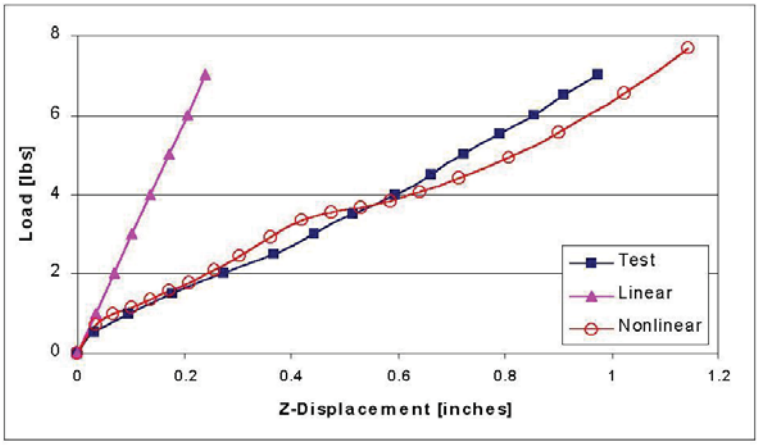

Figure 14: Load vs. displacement for case 1

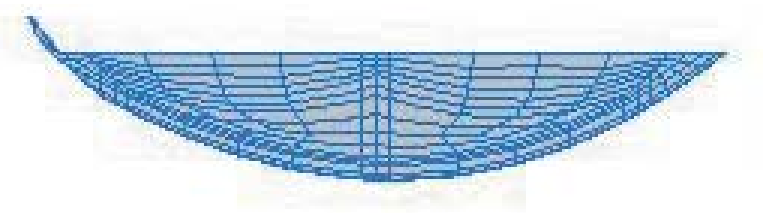

Figure 15: Deformed shape for case 1

The plot of the load vs. displacement at the load point is shown in Fig. 14. According to the test data, the displacement at the load point shows nonlinear behavior as the load increases. Initially, it shows a softening behavior and subsequently it begins to stiffen. The result of geometrically linear analysis is far off the test data, while the results of geometrically nonlinear analysis follow the test data reasonably well. The maximum displacement measured is approximately 1", which is about 30 times the dish thickness (0.032") at the load point.

In the experiment, the load was applied to the dish backside using a spherical end attachment on the load-cell, effectively applying a point load to the dish. To examine any effect of the differences in loading method on the structural response, an additional analysis was carried out using the total load distributed over the nodes around the original single load point. The results of this analysis were nearly identical to the single point load case.

Figure 15 shows the deformed shape of the reflector dish at a load slightly below 8 lbs. The computed displacements are exaggerated to clearly show the deformed shape around the load point.

4.2 Loading Case 2

As shown in Fig. 16, a special fine mesh is introduced around the load point to capture the local nonlinear behavior of the reflector.

According to the plot shown in Fig. 17, the experimental test data exhibits a nonlinear behavior. The displacement at the load point shows a softening behavior followed by a stiffening behavior as the applied load increases. The maximum displacement measured is approximately 0.85", which is very large compared with the thickness at the load point (0.016"). As in case 1, the geometrically linear analysis is inadequate, while the result of the geometrically nonlinear analysis follows the test data very well.

Figure 18 shows the deformed shape of the reflector dish at a load close to 8 lbs. The computed displacements are exaggerated to clearly show the deformed shape

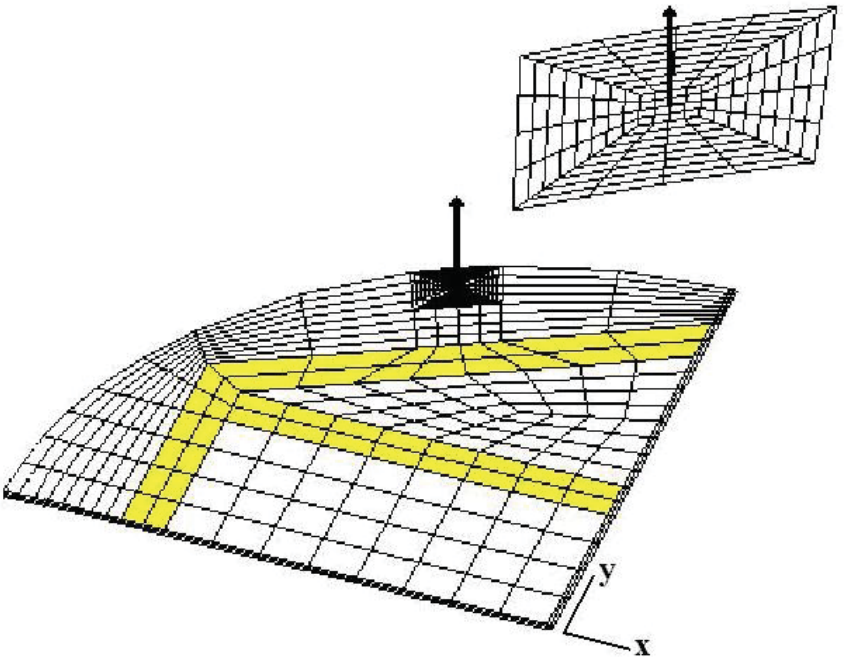

Figure 16: Load and mesh for case 2

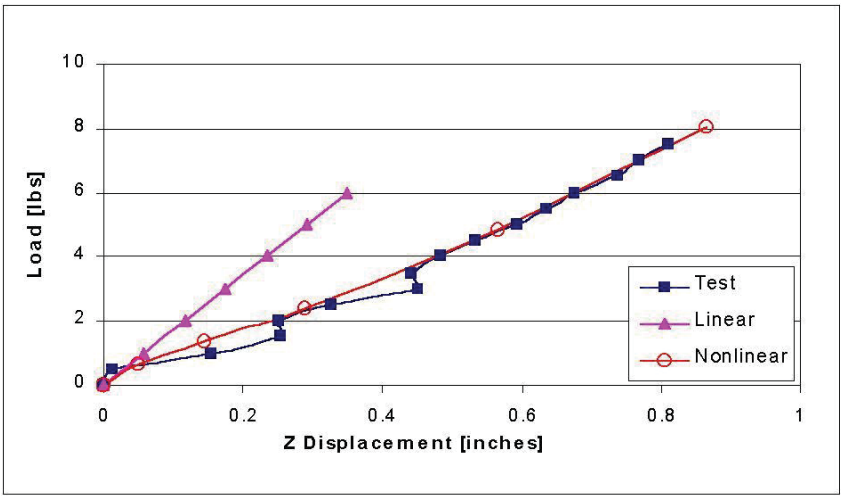

Figure 17: Load vs. displacement for case 2

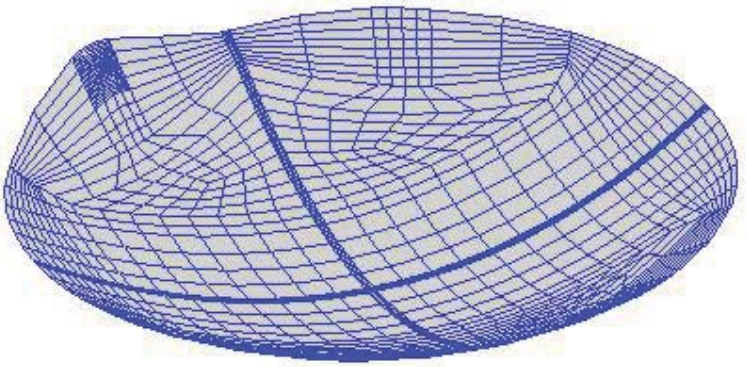

Figure 18: Deformed shape for case 2

around the load point.

4.3 Loading Case 3

A point load as shown in Fig. 19 is applied at a nodal point located in the doubly overlapped region, which is four times as thick as the non-overlapped area of the reflector dish. However, it is still very flexible as the zone is located far from the stiffeners.

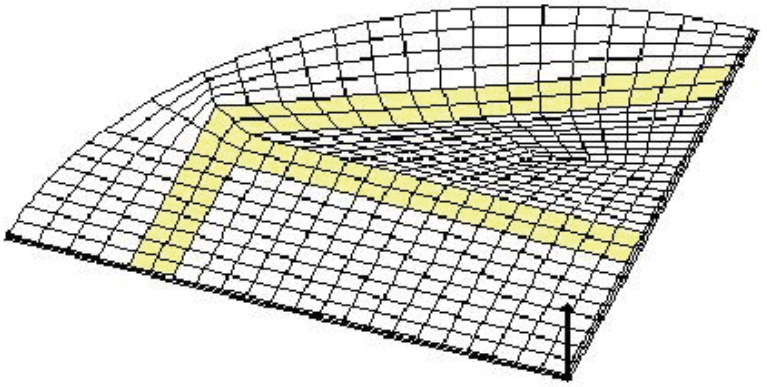

Figure 19: Load and mesh for case 3

According to the test data shown in Fig. 20, the displacement at the load point shows a highly nonlinear behavior, including the limit point as the applied load increases. The maximum displacement measured is approximately 0.45", which is

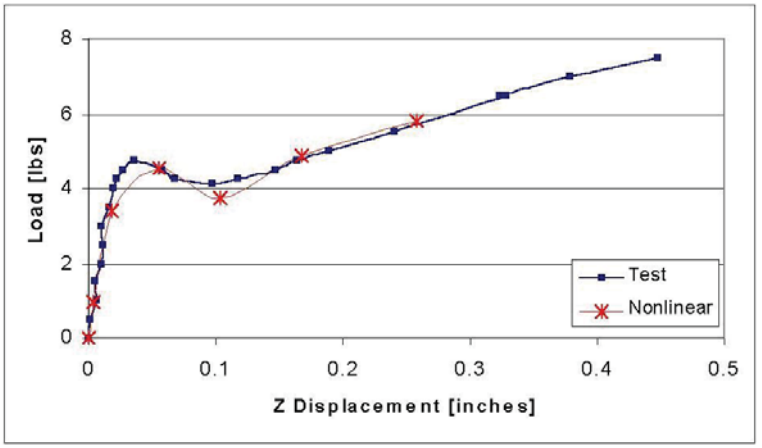

Figure 20: Load vs. displacement at the load point

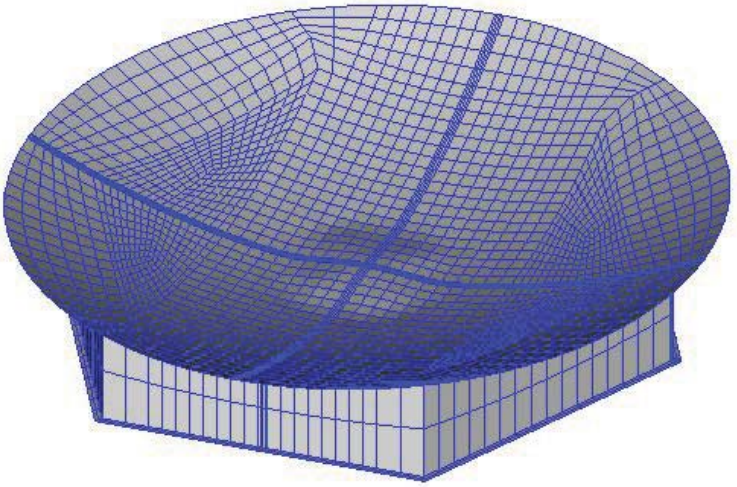

Figure 21: Deformed shape for case 3

large relative to the thickness at the load point (0.064"). The results of geometrically nonlinear analysis are in good agreement with the test data.

Figure 21 shows the deformed shape of the reflector dish at a load slightly below 6 lbs. The computed displacements are exaggerated to clearly show the deformed shape near the load point.

5 Conclusion

For the three load cases considered here, the results of geometrically nonlinear finite element analysis are in good agreement with the test data obtained from independently carried out experiments. This demonstrates that the present finite element approach, based on the assumed strain solid shell formulation, can be used for analysis of highly flexible structures such as a composite space reflector. Also, the results of numerical analysis and the experimental data reported in the present paper provide a benchmark for future investigations on the modeling and analysis of geometrically nonlinear composite shell structures via computational tools.

Acknowledgement The authors would like to thank Mr. Kenneth Segal of NASA Goddard Space Flight Center for the support of this work and Mr. Christopher Brown for providing the experimental data.

References

Ausserer, M.F.; Lee, S.W. (1988): An eighteen node solid element for thin shell analysis, *International Journal for Numerical Methods in Engineering*, Vol.26, pp. 1345-1364.

Chen, P. (1998): Telescope mirrors successfully lose weight, *Laser Focus World*, October, pp. 69-72.

Connell, S.J.; Abusafieh, A. (2002): Lightweight space mirrors from carbon fiber composites, *SAMPE Journal*, Vol. 38, No. 4, pp. 46-55.

Freeland, R.E.; McElroy, P.M. (1989): Technical approach for the development of structural composite mirrors, *SPIE Vol. 1114 Active Telescope Systems*, pp. 412-425.

Han, Z.D.; Rajendran, A.M.; Atluri, S.N. (2005): Meshless Local Petrov-Galerkin (MLPG) Approaches for Solving Nonlinear Problems with Large Deformations and Rotations, *CMES: Computer Modeling in Engineering & Sciences*, Vol. 10, no. 1, pp. 1-12.

Kemp, B.L.; Cho, C.; Lee, S.W. (1998): Four-Node Solid Shell Element Formulation with Assumed Strain, *International Journal for Numerical Methods in Engineering*, vol. 43, no. 5, pp. 909-924.

Kim, Y.H.; Lee, S.W. (1988): A Solid Element Formulation for Large Deflection Analysis of Composite Shell Structures, *Computers and Structures*, vol. 30, no. 1/2, pp. 269-274.

Lee, K.; Cho, C.; Lee S.W. (2002): A Geometrically nonlinear nine-node solid shell element formulation with reduced sensitivity to mesh distortion, *CMES: Computer Modeling in Engineering and Sciences,* Vol. 3, No. 3, pp. 339-349.

Lee, K.; Lee S.W. (2006): Analysis of gossamer space and near-space structures using assumed strain solid shell finite elements, *Journal of Spacecraft and Rockets*, Vol. 43, No. 6, pp. 1301-1307.

Lee, S.W.; Pian, T.H.H. (1978): Improvement of plate and shell finite element by mixed formulations, *AIAA Journal*, Vol. 16, pp. 29-34.

Park, H.C.; Cho, C.; Lee, S. W. (1995): An Efficient Assumed Strain Element Model with Six DOF per Node for Analysis of Geometrically Nonlinear Shells, *International Journal for Numerical Methods in Engineering*, vol. 38, no. 24, pp. 4101-4121.

Sladek, J.; Sladek, V.; Wen, P.H.; Aliabadi, M.H. (2006): Meshless Local Petrov-Galerkin (MLPG) Method for Shear Deformable Shells Analysis, *CMES: Computer Modeling in Engineering & Sciences*, Vol. 13, no. 2, pp. 103-117.

Tompkins, S.S.; Funk, J.G.; Bowles D.E.; Towell, T.W.; Connell, J.W. (1992): Composite materials for precision space reflector panels, *SPIE Vol. 1690 Design of Optical Instruments*, pp. 250-261.

Wen, P.H.; Hon, Y.C. (2007): Geometrically Nonlinear Analysis of Reissner-Mindlin Plate by Meshless Computation, *CMES: Computer Modeling in Engineering & Sciences*, Vol. 21, no. 3, pp. 177-191.